

Tricontrollable pixelated metasurface for absorbing terahertz radiation

*Pankaj Kumar*¹

Department of Electronics and Communication Engineering, National Institute of Technology Patna,
Patna 800005, Bihar, India

Akhlesh Lakhtakia

NanoMM—Nanoengineered Metamaterials Group, Department of Engineering Science and Mechanics, The
Pennsylvania State University, University Park, Pennsylvania 16802, USA

Material Architecture Center and Department of Electronics Engineering, Indian Institute of Technology
(BHU), Varanasi 221005, Uttar Pradesh, India

Sektion for Konstruktion og Produktudvikling, Institut for Mekanisk Teknologi, Danmarks Tekniske
Universitet, DK-2800 Kongens Lyngby, Danmark

Pradip K. Jain

Department of Electronics and Communication Engineering, National Institute of Technology Patna,
Patna 800005, Bihar, India

Material Architecture Center and Department of Electronics Engineering, Indian Institute of Technology
(BHU), Varanasi 221005, Uttar Pradesh, India

Abstract. The incorporation of materials with controllable electromagnetic constitutive parameters allows the conceptualization and realization of controllable metasurfaces. With the aim of formulating and investigating a tricontrollable metasurface for efficiently absorbing terahertz radiation, we adopted a pixel-based approach in which the meta-atoms are biperiodic assemblies of discrete pixels. We patched some pixels with indium antimonide (InSb) and some with graphene, leaving the others unpatched. The bottom of each meta-atom was taken to comprise a metal-backed substrate of silicon nitride. The InSb-patched pixels facilitate the thermal and magnetic control modalities, whereas the graphene-patched pixels facilitate the electrical control modality. With proper configuration of patched and unpatched pixels and with proper selection of the patching material for each patched pixel, the absorptance spectrums of the pixelated metasurface were found to contain peak-shaped features with maximum absorptance exceeding 0.95, full-width-at-half-maximum bandwidth of less than 0.7 THz, and the maximum-absorptance frequency lying between 2 THz and 4 THz. The location of the maximum-absorptance frequency can be thermally, magnetically, and electrically controllable. The lack of rotational invariance of the optimal meta-atom adds mechanical rotation as the fourth control modality.

1 Introduction

A metasurface is conceptualized as a planar periodic array of identical, electrically thin meta-atoms whose lateral extent is a small fraction of the free-space wavelength λ_0 [1]. After relaxing the length restriction, the foregoing description applies even to many gradient metasurfaces [2] without any need to generalize the standard laws of reflection and refraction of plane waves [3, 4]. Although metasurfaces have been designed and fabricated for application in spectral regimes ranging from the radio to the visible frequencies [5, 6], they are particularly attractive for terahertz applications [7, 8, 9] that include imaging [10], spectroscopy [11], and cancer detection [12].

Absorption of terahertz radiation by metasurfaces is an area of ongoing research [13, 15, 14, 16, 17, 18]. In many of these metasurface absorbers, the meta-atom comprises graphene on a dielectric substrate backed by a metal [13, 14, 17]. The frequency-dependent surface conductivity σ_{gr} of graphene [19] can be fixed by

¹Corresponding author: pankajjha@nitp.ac.in

substitutional doping [20]. More importantly, σ_{gr} can be dynamically controlled by varying the chemical potential μ_{ch} of graphene, with the application of a quasistatic electric field [22, 21] and/or a quasistatic magnetic field [23, 21]. Accordingly, the spectrum of the absorptance A of a metasurface containing graphene [14, 17] can be dynamically controlled.

The application of a quasistatic electric field E_{dc} (in V nm^{-1}) along a fixed direction provides a convenient control modality. For more reliable operation, an additional control modality would be desirable. At first glance, the absolute temperature T (in K) appears promising as the second control modality because the temperature-dependent Fermi–Dirac distribution [24] is present in both

- the Kubo formula for σ_{gr} [Eq. (1.34), Ref. [19]] and
- the Hanson formula for μ_{ch} [Eq. (53), Ref. [21]].

However, the overall temperature-dependence is so weak for $T \in [273, 323]$ K as to be inconsequential. This means that a different material, with strongly temperature-dependent dielectric properties, must be incorporated along with graphene in the meta-atoms.

Indium antimonide (InSb) is a promising material for this purpose. An isotropic n -type semiconductor, InSb has free carriers with low effective mass so that its conductivity can be thermally controlled [25, 26]. When subjected to a quasistatic magnetic field B_0 (in T) along a fixed direction, InSb exhibits the uniaxial gyrotropic characteristics of a magnetoplasma [27, 28]. Thus, InSb’s magnetothermally dependent dielectric properties provide two additional control modalities in the terahertz regime [29].

Parenthetically, multicontrollability abounds in nature. At different stages in our lives, we use different sets of muscles to move from one location to another. A message can be transmitted by one person to another by writing as well as by speaking; likewise, a message can be received by a person visually as well as aurally. In critical facilities—such as nuclear power plants, space stations, and missile guidance and command centers—multiple control modalities are used to reliably effect specific actions. As terahertz systems are being increasingly used for diverse applications, multicontrollability will be appreciated and even required in diverse scenarios.

In this paper, we propose and simulate a tricontrollable metasurface for efficiently absorbing terahertz radiation. Each meta-atom of this metasurface is made up of pixels [17, 30, 32, 31] affixed to a metal-backed dielectric substrate. Some pixels are patched with InSb, some with graphene, and the remaining ones are unpatched. The pixellation of the metasurface permits trimodal control of the frequency of maximum absorptance. The proposed absorber is also polarization insensitive.

The plan of this paper is as follows. Section 2 provides descriptions of the T - and B_0 -dependences of the relative permittivity of InSb, the E_{dc} -dependence of the surface conductivity of graphene, the proposed metasurface, and the boundary-value problem solved to determine the absorptance of the metasurface when illuminated by a plane wave. Section 3 provides a discussion of numerical results obtained by us. The paper concludes with some remarks in Sec. 4.

An $\exp(-i\omega t)$ dependence on time t is implicit, with $i = \sqrt{-1}$, $\omega = 2\pi f$ as the angular frequency, and f as the linear frequency. The free-space wavenumber is denoted by $k_o = \omega\sqrt{\varepsilon_o\mu_o} = 2\pi/\lambda_o$, where ε_o is the permittivity and μ_o is the permeability of free space. Vectors are denoted by boldface letters; the Cartesian unit vectors are denoted by $\hat{\mathbf{x}}$, $\hat{\mathbf{y}}$, and $\hat{\mathbf{z}}$; and dyadics are double underlined.

2 Materials and Methods

2.1 Pixellated meta-atom

The metasurface is infinitely extended along the x and y axes, with the z axis normal to it. The metasurface is biperiodic in the xy plane, with each meta-atom taken to be a square of side $a \leq \lambda_c/4$ in that plane, with λ_c being the lowest operational value of λ_o . The bottom of each meta-atom is a metal-backed dielectric substrate, as shown in Fig. 1. The thickness and the relative permittivity scalar of the substrate are denoted by L_{sub} and ε_{sub} , respectively; and those of the metal by L_{met} and ε_{met} , respectively.

On top of the substrate in each meta-atom, an inner square of side $a - d$, $d \ll a$, is partitioned into square pixels of side b , with each pixel separated from its nearest neighbor on every side by a strip of thickness d . The dimensions b and d must be selected so that the ratio $N_r = a/(b + d)$ is an integer. The number of pixels in the meta-atom is thus $N_{\max} = N_r^2$. The pixels are aligned along the x and y axes. Some pixels are patched with InSb, some patched with graphene, and the remaining ones are unpatched.

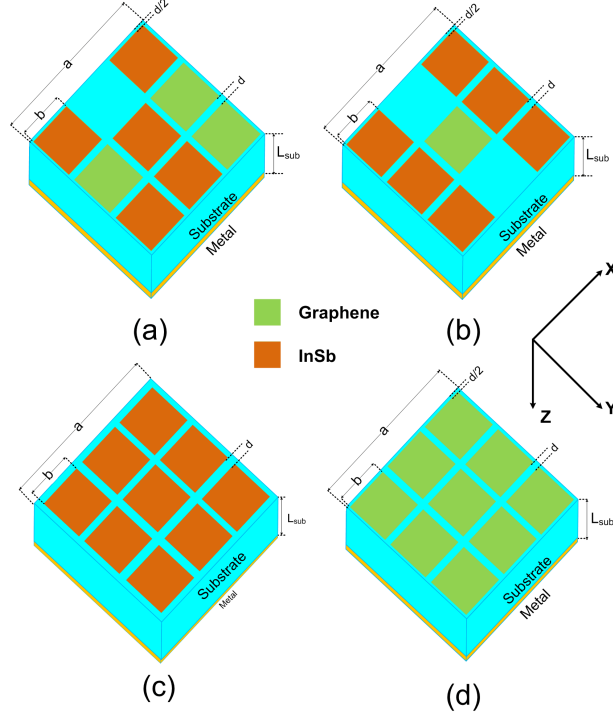


Figure 1: (a) Schematic of a meta-atom comprising $N_{\max} = 3 \times 3$ pixels, some patched with InSb, some patched with graphene, and the remaining unpatched, on top of a metal-backed dielectric substrate. (b) Schematic of a meta-atom with one pixel patched with graphene, six patched with InSb, and two unpatched. (c and d) Schematics of meta-atoms with (c) all pixels patched with InSb and (d) all pixels patched with graphene.

2.2 Relative permittivity of InSb

When a quasistatic magnetic field $B_0 \hat{\mathbf{x}}$ is applied, the relative permittivity dyadic $\underline{\underline{\epsilon}}_{\text{InSb}}$ of InSb in the terahertz spectral regime can be stated in matrix form as [28]

$$\underline{\underline{\epsilon}}_{\text{InSb}} = \begin{pmatrix} \epsilon_{\text{InSb}}^{\text{xx}} & 0 & 0 \\ 0 & \epsilon_{\text{InSb}}^{\text{yy}} & \epsilon_{\text{InSb}}^{\text{yz}} \\ 0 & \epsilon_{\text{InSb}}^{\text{zy}} & \epsilon_{\text{InSb}}^{\text{zz}} \end{pmatrix}, \quad (1)$$

where [29]

$$\epsilon_{\text{InSb}}^{\text{xx}} = \epsilon_{\text{InSb}}^{(\infty)} - q_e^2 \left(\frac{N_{\text{InSb}}}{\omega \epsilon_o m_{\text{InSb}}} \right) \frac{1}{\omega + i\gamma_{\text{InSb}}}, \quad (2)$$

$$\begin{aligned}\varepsilon_{\text{InSb}}^{\text{yy}} = \varepsilon_{\text{InSb}}^{\text{zz}} &= \varepsilon_{\text{InSb}}^{(\infty)} - q_e^2 \left(\frac{N_{\text{InSb}}}{\omega \varepsilon_o m_{\text{InSb}}} \right) \\ &\times \frac{\omega + i\gamma_{\text{InSb}}}{(\omega + i\gamma_{\text{InSb}})^2 - \left(\frac{q_e B_0}{m_{\text{InSb}}} \right)^2},\end{aligned}\quad (3)$$

and

$$\begin{aligned}\varepsilon_{\text{InSb}}^{\text{zy}} = -\varepsilon_{\text{InSb}}^{\text{yz}} &= -iq_e^2 \left(\frac{N_{\text{InSb}}}{\omega \varepsilon_o m_{\text{InSb}}} \right) \\ &\times \left(\frac{q_e B_0}{m_{\text{InSb}}} \right) \frac{1}{(\omega + i\gamma_{\text{InSb}})^2 - \left(\frac{q_e B_0}{m_{\text{InSb}}} \right)^2}.\end{aligned}\quad (4)$$

Here, $\varepsilon_{\text{InSb}}^{(\infty)} = 15.68$ is the high-frequency part, $m_{\text{InSb}} = 0.015m_e$, $m_e = 9.109 \times 10^{-31}$ kg is the mass of an electron, $q_e = -1.602 \times 10^{-19}$ C is the charge of an electron, $\gamma_{\text{InSb}} = \pi \times 10^{11}$ rad s⁻¹ is the damping constant,

$$N_{\text{InSb}} = 5.76 \times 10^{20} T^{3/2} \exp(-\mathcal{E}_g/2k_B T) \quad (5)$$

is the temperature-dependent intrinsic carrier density (in m⁻³), $\mathcal{E}_g = 0.26$ eV is the bandgap energy, and $k_B = 8.617 \times 10^{-5}$ eV K⁻¹ is the Boltzmann constant [25, 26, 29].

Components of $\underline{\varepsilon}_{\text{InSb}}$ are shown as functions of $B_0 \in [-1, 1]$ T and $T \in [270, 320]$ K in Fig. 2. As is clear from Eqs. (2)–(4), reversal of the sign of B_0 affects only the two off-diagonal components of $\underline{\varepsilon}_{\text{InSb}}$. That effect is an interchange of $\varepsilon_{\text{InSb}}^{\text{zy}}$ and $\varepsilon_{\text{InSb}}^{\text{yz}}$, but it cannot have a major consequence as the off-diagonal components are very small compared to the diagonal components of $\underline{\varepsilon}_{\text{InSb}}$.

2.3 Surface conductivity of graphene

As a 0.335-nm-thick layer, graphene is modeled as an infinitesimally thin sheet with surface conductivity [Eq. (1.34), Ref. [19]]

$$\begin{aligned}\sigma_{\text{gr}} &= -\frac{q_e^2 \tau_{\text{gr}} (1 - i\omega \tau_{\text{gr}})}{\pi \hbar^2} \left[\int_{-\infty}^{\infty} \frac{|\mathcal{E}|}{(1 - i\omega \tau_{\text{gr}})^2} \frac{\partial F(\mathcal{E}, \mu_{\text{ch}})}{\partial \mathcal{E}} d\mathcal{E} \right. \\ &\quad \left. + \int_0^{\infty} \frac{F(\mathcal{E}, \mu_{\text{ch}}) - F(-\mathcal{E}, \mu_{\text{ch}})}{(1 - i\omega \tau_{\text{gr}})^2 + 4\tau_{\text{gr}}^2 \mathcal{E}^2 / \hbar^2} d\mathcal{E} \right],\end{aligned}\quad (6)$$

where the momentum relaxation time τ_{gr} is assumed to be independent of the energy \mathcal{E} ,

$$F(\mathcal{E}, \mu_{\text{ch}}) = \left[1 + \exp \left(\frac{\mathcal{E} - \mu_{\text{ch}}}{k_B T} \right) \right]^{-1} \quad (7)$$

is the Fermi–Dirac distribution function [24], and $\hbar = 6.582 \times 10^{-16}$ eV rad⁻¹ s is the reduced Planck constant.

Under the influence of $E_{\text{dc}} \hat{\mathbf{z}}$, which is directed normally to graphene, the chemical potential μ_{ch} is a solution of the equation [21, Eq. (53), Ref.]

$$E_{\text{dc}} = \frac{q_e}{\pi \varepsilon_o \varepsilon_{\text{dc}} \hbar^2 v_F^2} \int_0^{\infty} \mathcal{E} [F(\mathcal{E}, \mu_{\text{ch}}) - F(\mathcal{E} + 2\mu_{\text{ch}}, \mu_{\text{ch}})] d\mathcal{E}, \quad (8)$$

where v_F is the Fermi speed of graphene and ε_{dc} is the dc relative permittivity of the substrate. The integral on the right side of Eq. (8) can be determined analytically to yield

$$\frac{\pi \varepsilon_o \varepsilon_{\text{dc}} \hbar^2 v_F^2 E_{\text{dc}}}{q_e k_B^2 T^2} = \text{Li}_2 \left[-\exp \left(-\frac{\mu_{\text{ch}}}{k_B T} \right) \right] - \text{Li}_2 \left[-\exp \left(\frac{\mu_{\text{ch}}}{k_B T} \right) \right], \quad (9)$$

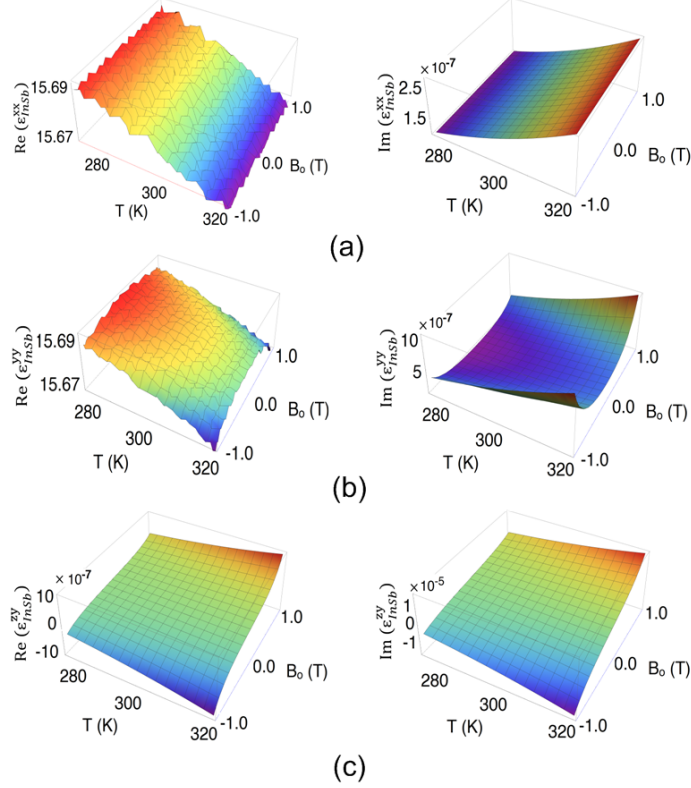


Figure 2: Real and imaginary parts of (a) $\epsilon_{\text{InSb}}^{xx}$, (b) $\epsilon_{\text{InSb}}^{yy}$, and (c) $\epsilon_{\text{InSb}}^{zy}$ as functions of $B_0 \in [-1, 1]$ T and $T \in [270, 320]$ K.

where $\text{Li}_\nu(\zeta)$ is the polylogarithm function of order ν and argument ζ [33]. The Newton–Raphson technique [34] can be used to determine μ_{ch} as a function of E_{dc} . Reversal of the sign of μ_{ch} reverses the sign of E_{dc} , according to Eqs. (8) and (9). Graphene is not affected significantly by $B_0 \hat{\mathbf{x}}$, because that quasistatic magnetic field is wholly aligned in the plane containing the carbon atoms [21].

We fixed $v_F = 10^6 \text{ m s}^{-1}$ [35] and $\tau_{\text{gr}} = 1 \text{ ps}$ [36]. Taking chemically prepared silicon nitride (SiN_x) as the substrate [37], we set $\epsilon_{\text{dc}} = 7.5$ [38] and solved Eq. (9) to determine μ_{ch} as a function of E_{dc} for $T \in \{270, 280, 290, 300, 310, 320\}$ K. Figure 3a shows μ_{ch} as a function of $E_{\text{dc}} \in [-0.08, 0.08] \text{ V nm}^{-1}$ and $T \in [270, 320]$ K. Detailed examination of this figure reveals that μ_{ch} is practically independent of temperature for $T \in [270, 320]$ K; thus, σ_{gr} is also temperature independent in the same temperature range. As expected from Eq. (8), reversal of the sign of E_{dc} reverses the sign of μ_{ch} in Fig. 3a.

Figures 3b and 3c, respectively, show the spectrums of the real and imaginary parts of σ_{gr} in relation to $E_{\text{dc}} \in [-0.08, 0.08] \text{ V nm}^{-1}$ for $T = 300 \text{ K}$. Clearly, σ_{gr} is unaffected by the sign of E_{dc} .

2.4 Plane-wave response

The illumination of the pixelated metasurface by a normally incident, linearly polarized, plane wave was investigated. The incident electric field phasor is then given by

$$\mathbf{E}_{\text{inc}} = (-\hat{\mathbf{x}} \cos \varphi + \hat{\mathbf{y}} \sin \varphi) \exp(ik_o z) \quad (10)$$

and the incident magnetic field phasor by

$$\mathbf{H}_{\text{inc}} = -\eta_o^{-1} (\hat{\mathbf{x}} \sin \varphi + \hat{\mathbf{y}} \cos \varphi) \exp(ik_o z), \quad (11)$$

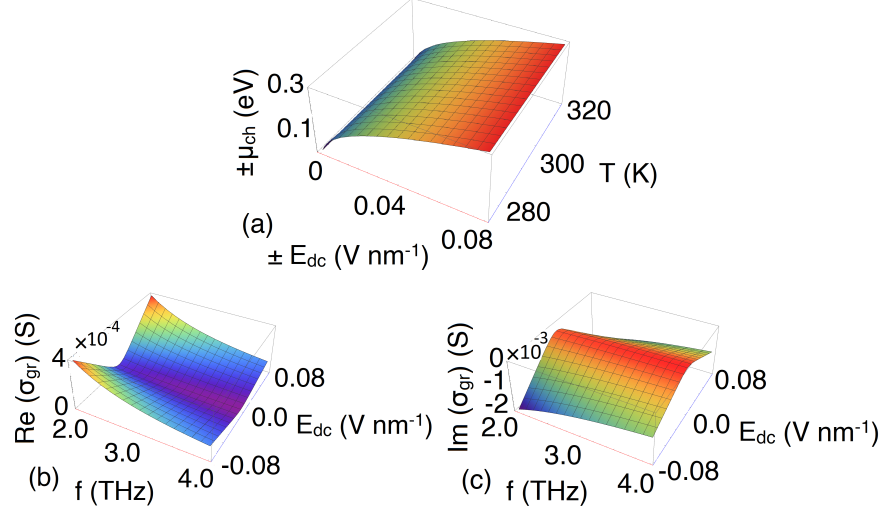


Figure 3: (a) μ_{ch} as a function of $E_{\text{dc}} \in [-0.08, 0.08]$ V nm $^{-1}$ and $T \in [270, 320]$ K, when $\varepsilon_{\text{dc}} = 7.5$. Note that the signs of μ_{ch} and E_{dc} have to be the same. (b) Real and (c) imaginary parts of σ_{gr} as functions of $f \in [2, 4]$ THz and $E_{\text{dc}} \in [-0.08, 0.08]$ V nm $^{-1}$, when $\varepsilon_{\text{dc}} = 7.5$ and $T = 300$ K.

where $\eta_o = \sqrt{\mu_o/\varepsilon_o}$ is the intrinsic impedance of free space and $\varphi \in [0^\circ, 90^\circ]$ is the polarization angle. The plane wave is transverse-electric [39] or perpendicularly polarized [40] when $\varphi = 90^\circ$ and transverse-magnetic [39] or parallel polarized [40] when $\varphi = 0^\circ$. The substrate SiN $_x$ was taken to be nondispersive and slightly dissipative in the 2–4-THz spectral regime; thus, $\varepsilon_{\text{sub}} = 7.6 + i0.06$ [41]. The metal backing the substrate was taken to be copper [36] with conductivity 5.9×10^7 S m $^{-1}$, the thickness $L_{\text{met}} = 0.2$ μm being several times larger than the skin depth ($= 0.046$ μm [39]) in order to prevent transmission through the metasurface.

In order to determine the reflected and transmitted electric and magnetic fields, a 3D full-wave simulation in the 2–4-THz spectral regime was carried out using the commercially available CST Microwave StudioTM 2019 software. Because of periodicity along the x and y axes, the 2D Floquet model was used for the simulation. Adaptive refinement of a mesh of tetrahedrons was done, with the number of tetrahedrons being 47844 for the meta-atom depicted in Fig. 1a, 16413 for Fig. 1b, 17523 for Fig. 1c, and 52123 for Fig. 1d. Being very thin, a graphene patch requires many more tetrahedrons than an InSb patch of the same lateral dimensions.

Transmission was found to be infinitesimal, as expected. The reflected electromagnetic field contained both co-polarized and cross-polarized components, in general. A post-processing module was used to compute the absorptance A , as explained elsewhere [42], by making use of the principle of conservation of energy and subtracting the sum of the co- and cross-polarized reflectances from unity.

3 Numerical Results and Discussion

Numerous different meta-atoms can be configured when $N_r > 2$ and the placement and the numbers of InSb-patched, graphene-patched, and unpatched pixels are varied. The temperature dependence of σ_{gr} is extremely weak for $T \in [270, 320]$ K, graphene is unaffected by the application of quasistatic magnetic field oriented tangentially to it, whereas $\varepsilon_{\text{InSb}}$ is unaffected by $|E_{\text{dc}}| \leq 0.08$ V nm $^{-1}$. However, σ_{gr} depends so strongly on E_{dc} that even a few graphene-patched pixels can overwhelm the magnetothermal control provided by the InSb-patched pixels.

We fixed $a = 9.6$ μm , $b = 3$ μm , $d = 0.2$ μm , and $L_{\text{sub}} = 9.6$ μm , based on experience [17]. After visually examining results obtained with all configurations possible when $N_r = 3$, we settled on the configuration shown in Fig. 1b: a single graphene-patched pixel accompanied by six InSb-patched and two unpatched

pixels. For comparison, we also calculated the spectrums of A for meta-atoms with either all nine InSb-patched pixels, as shown in Fig. 1c, or all nine graphene-patched pixels, as shown in Fig. 1d.

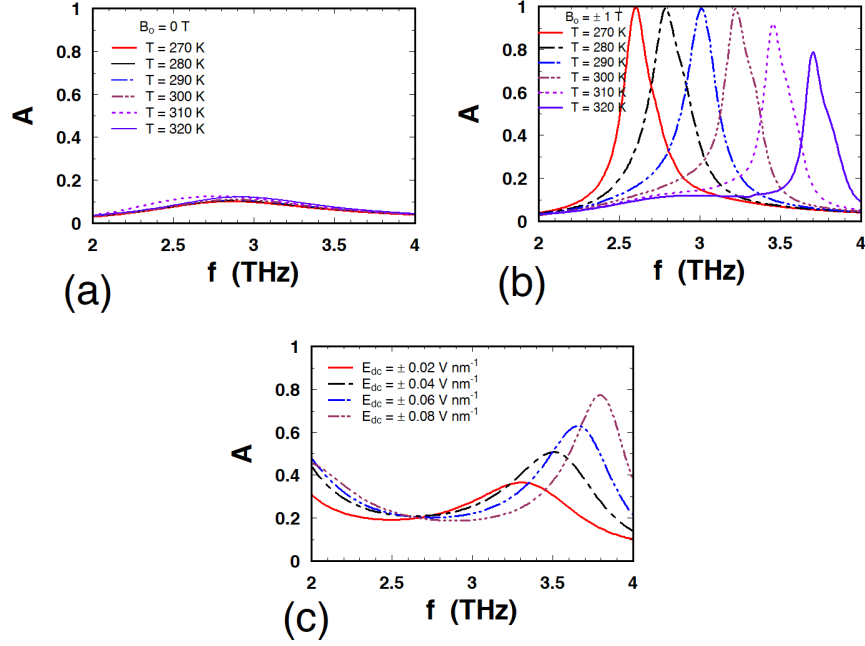


Figure 4: (a and b) Absorptance spectrums of a metasurface with all nine pixels patched with InSb (Fig. 1c) for $T \in \{270, 280, 290, 300, 310, 320\}$ K when $\varphi = 0^\circ$ and (a) $B_0 = 0$ and (b) $B_0 = \pm 1$ T. (c) Absorptance spectrums of a metasurface with all nine pixels patched with graphene (Fig. 1d) for $E_{dc} \in \{\pm 0.02, \pm 0.04, \pm 0.06, \pm 0.08\}$ V nm $^{-1}$, when $T = 300$ K and $\varphi = 0^\circ$.

3.1 Thermal control modality

The thermal control modality is demonstrated in Fig. 4a containing the spectrums of absorptance A when all nine pixels are patched with InSb (Fig. 1c), $B_0 = 0$, and T changes from 270 K to 320 K in steps of 10 K, the value of $|E_{dc}| \leq 0.08$ V nm $^{-1}$ being irrelevant. The illuminating plane wave was taken to be normally incident with $\mathbf{E}_{inc} \parallel \hat{\mathbf{x}}$ for calculations.

Each of the six absorptance spectrums contains a very broad peak-shaped feature with a maximum absorptance that lies between 0.10 and 0.12. The maximum-absorptance frequency does change from 2.86 THz to 2.92 THz at the rate of 1.2 GHz K $^{-1}$ as the temperature increases from 270 K to 320 K, but the controllability provided by temperature alone is modest at best.

The absorptance peaks narrow considerably and the maximum absorptances increase in Fig. 4b when $|B_0|$ is increased to 1 T. Although the sign of B_0 does affect ε_{InSb}^{zy} , neither ε_{InSb}^{xx} nor ε_{InSb}^{yy} are affected by it. But, as the off-diagonal components of $\underline{\underline{\varepsilon}}_{InSb}$ are not of significant magnitude compared to the diagonal components of $\underline{\underline{\varepsilon}}_{InSb}$, in the remainder of this paper we have ignored the minuscule dependence of A on the sign of B_0 .

As T increases from 270 K to 320 K in Fig. 4b, the maximum-absorptance frequency blueshifts at the rate of ~ 0.02 THz K $^{-1}$ from 2.59 THz to 3.68 THz and the maximum absorptance first increases slowly from 0.96 to 0.985 (at $T = 290$ K) and then decreases rapidly to 0.69 (at $T = 320$ K). The full-width-at-half-maximum (FWHM) bandwidth lies between 0.19 and 0.24 THz for $T \leq 300$ K, but drops to 0.15 THz at $T = 310$ K and 0.09 THz at $T = 320$ K. Thus, we conclude from Figs. 4a and 4b that thermal control of InSb-patched pixels should be more effective when a quasistatic magnetic field of sufficiently large magnitude is also applied.

3.2 Magnetic control modality

The magnetic control modality due to InSb-patched pixels is revealed by a comparison of Figs. 4a and 4b. Increase of $|B_0|$ from 0 to 1 T causes the maximum-absorptance frequency to

- (i) redshift by 0.27 THz at $T = 270$ K and 0.09 THz at $T = 280$ K, and
- (ii) blueshift by 0.10 THz at $T = 290$ K, 0.31 THz at $T = 300$ K, 0.53 THz at $T = 310$ K, and 0.76 THz at $T = 320$ K.

Simultaneously, the increase of $|B_0|$ enhances the maximum absorptance from low values (0.11 ± 0.01) to values exceeding 0.68 and as high as 0.985. A reversal of the sign of B_0 is infructuous, for the reasons discussed in Sec. 3.3.1.

3.3 Electrical control modality

The electrical control modality is demonstrated in Fig. 4c containing the absorptance spectrums when all nine pixels are patched with graphene (Fig. 1d) and $|E_{dc}|$ changes from 0.02 V nm^{-1} to 0.08 V nm^{-1} in steps of 0.02 V nm^{-1} , the values of B_0 and $T \in [270, 320]$ K being irrelevant. The calculations were made for a normally incident plane wave with $\mathbf{E}_{inc} \parallel \hat{\mathbf{x}}$.

As is clear from Figs. 3b and 3c, reversal of the sign of E_{dc} does not affect σ_{gr} ; hence, A is unaffected by the sign of E_{dc} . Each of the four absorptance spectrums in Fig. 4c contains a prominent peak-shaped feature. As $|E_{dc}|$ increases from 0.02 V nm^{-1} to 0.08 V nm^{-1} , the FWHM bandwidth decreases, the maximum-absorptance frequency blueshifts from 3.29 THz to 3.79 THz at the rate of about $8.3 \text{ THz V}^{-1} \text{ nm}$, and the maximum absorptance rises from 0.35 to 0.78. The modest values of the maximum absorptance are not surprising because graphene by itself is a modest absorber of low-THz radiation [43], although properly designed graphene metasurfaces can deliver almost the maximum absorptance possible [17, 44, 45].

3.4 Tricontrollable metasurface

Having confirmed the bicontrollability of InSb-patched pixels in Secs. 3.3.1 and 3.3.2 and the unicontrollability of graphene-patched pixels in Secs. 3.3.3, we now move on to the metasurface depicted in Fig. 1b: each meta-atom has its central pixel patched with graphene, six pixels patched with InSb, and two unpatched pixels.

The absorptance A was calculated for a normally incident plane wave with $\mathbf{E}_{inc} \parallel \hat{\mathbf{x}}$. Figures 5a–i show A as a function of $f \in [2, 4] \text{ THz}$ and $T \in [270, 320] \text{ K}$ for nine combinations of $|B_0|$ and $|E_{dc}|$.

3.4.1 $B_0 = 0$

Let us begin with $B_0 = 0$. Figures 5a–c show a peak-shaped feature in the absorptance spectrum, with the maximum absorptance lying between 0.93 and 0.99 and the FWHM bandwidth between 0.28 THz and 0.48 THz. Clearly, thermal control provided by the six InSb-patched pixels is weak, the maximum-absorptance frequency blueshifting at the rate of about $0.0012 \text{ THz K}^{-1}$. The weakness of thermal control in the absence of a quasistatic magnetic field follows from Sec. 3.3.1.

However, the electrical control modality provided by the sole graphene-patched pixel is strong in Figs. 5a–c. As $|E_{dc}|$ increases from 0.02 V nm^{-1} to 0.08 V nm^{-1} , the FWHM bandwidth decreases and the maximum-absorptance frequency blueshifts at the rate of about $18.66 \text{ THz V}^{-1} \text{ nm}$.

3.4.2 $|B_0| > 0$

The introduction of $|B_0| > 0$ of a sufficiently large magnitude creates a second peak-shaped feature in the absorptance spectrum, as is evident in Figs. 5d–i. Whereas the first feature remains almost temperature independent, the second feature is strongly dependent on temperature.

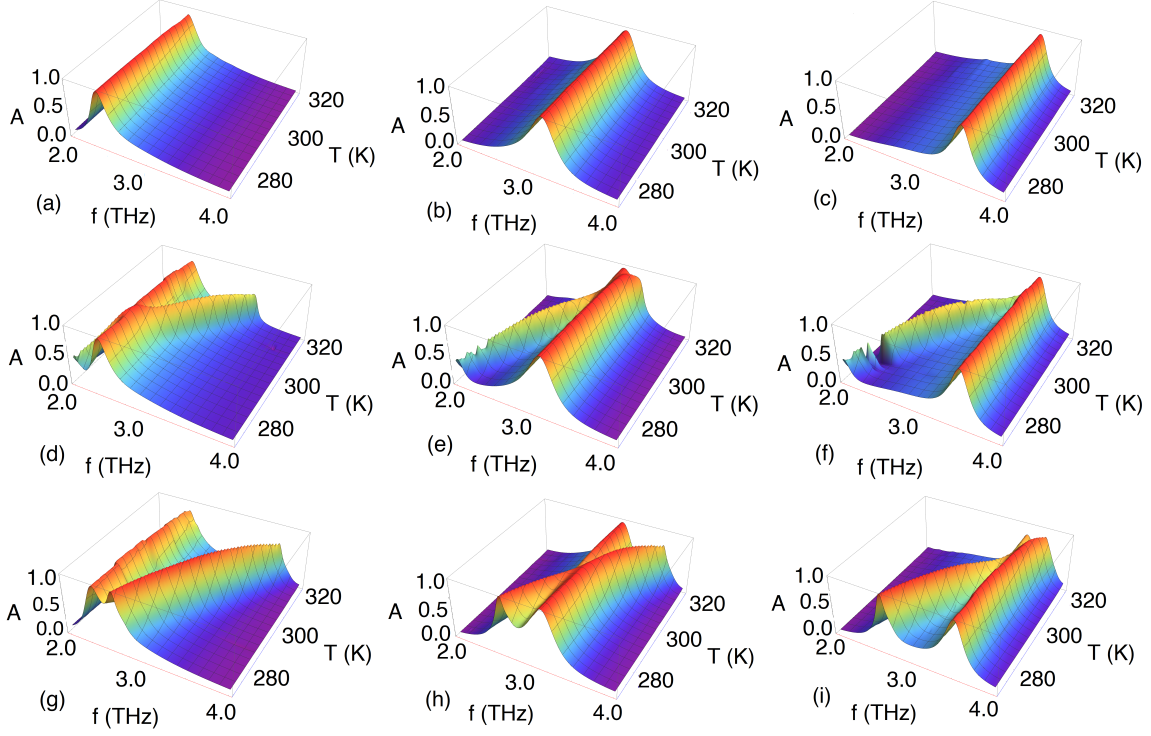


Figure 5: Absorbance A of the metasurface depicted via Fig. 1b as a function of $f \in [2, 4]$ THz and $T \in [270, 320]$ K, when $\varphi = 0^\circ$. (a–c) $B_0 = 0$ with (a) $|E_{dc}| = 0.02$ V nm $^{-1}$, (b) $|E_{dc}| = 0.05$ V nm $^{-1}$, and (c) $|E_{dc}| = 0.08$ V nm $^{-1}$; (d–f) $|B_0| = 0.5$ T with (d) $|E_{dc}| = 0.02$ V nm $^{-1}$, (e) $|E_{dc}| = 0.05$ V nm $^{-1}$, and (f) $|E_{dc}| = 0.08$ V nm $^{-1}$; and (g–i) $|B_0| = 1$ T with (g) $|E_{dc}| = 0.02$ V nm $^{-1}$, (h) $|E_{dc}| = 0.05$ V nm $^{-1}$, and (i) $|E_{dc}| = 0.08$ V nm $^{-1}$.

1st peak-shaped feature

Let us first discuss the peak-shaped feature that is very weakly dependent on temperature. A comparison of the three graphs in any column of Fig. 5 shows that feature is also weakly dependent on the quasistatic magnetic field. For $|E_{dc}| = 0.02$ V nm $^{-1}$ and $T = 310$ K, a comparison of Figs. 5a, 5d, and 5g shows that the maximum-absorbance frequency redshifts from 2.41 THz to 2.38 THz at the rate of about 0.03 THz T $^{-1}$, as $|B_0|$ is increased from 0 to 1 T. For $|E_{dc}| = 0.08$ V nm $^{-1}$ and $T = 310$ K, a comparison of Figs. 5c, 5f, and 5i shows that the maximum-absorbance frequency blueshifts from 3.52 THz to 3.57 THz at the rate of about 0.05 THz T $^{-1}$, as $|B_0|$ is increased from 0 to 1 T. These spectral shifts are evident in the absorption spectrums provided in Fig. 6.

However, if $|B_0|$ is fixed between 0 and 1 T, a quasistatic electric field can be used to blueshift the maximum-absorbance frequency at the rate of about 19.1 THz V $^{-1}$ nm. Thus, the 1st peak-shaped feature is controlled primarily by a quasistatic electric field that acts through the graphene-patched pixel.

2nd peak-shaped feature

The second peak-shaped feature is absent for $B_0 = 0$ and it is also strongly dependent on temperature. Thus, it surely arises from the bicontrollability of the six InSb-patched pixels. The magnetic control modality becomes obvious on comparing Figs. 5d and 5g, for both of which $|E_{dc}| = 0.02$ V nm $^{-1}$. In addition, electric control can be strongly exerted through the sole graphene-patched pixel, as is clear on comparing Figs. 5h and 5i, for both of which $|B_0| = 1$ T.

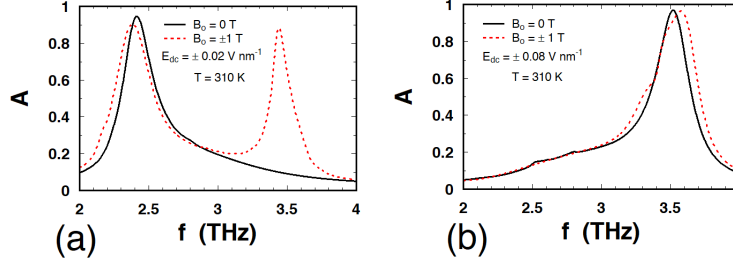


Figure 6: Absorbance A of the metasurface depicted via Fig. 1b as a function of $f \in [2, 4]$ THz for $|B_0| \in \{0, 1\}$ T at $T = 310$ K, when $\varphi = 0^\circ$ and (a) $|E_{dc}| = 0.02$ V nm $^{-1}$ and (b) $|E_{dc}| = 0.08$ V nm $^{-1}$.

3.4.3 Example No. 1

An example presented through Fig. 7 allows appreciation of tricontrollability quite easily. Suppose that the quiescent conditions for the operation of the metasurface depicted via Fig. 1b are as follows: $T = 290$ K, $|B_0| = 0.9$ T, and $|E_{dc}| = 0.07$ V nm $^{-1}$. Then, as shown through the black solid curves in Fig. 7, the absorbance spectrum contains both peak-shaped features. The low-frequency feature has a maximum-absorbance frequency of 2.87 THz and FWHM bandwidth of 0.28 THz. The high-frequency feature has a maximum-absorbance frequency of 3.39 THz and FWHM bandwidth of 0.38 THz.

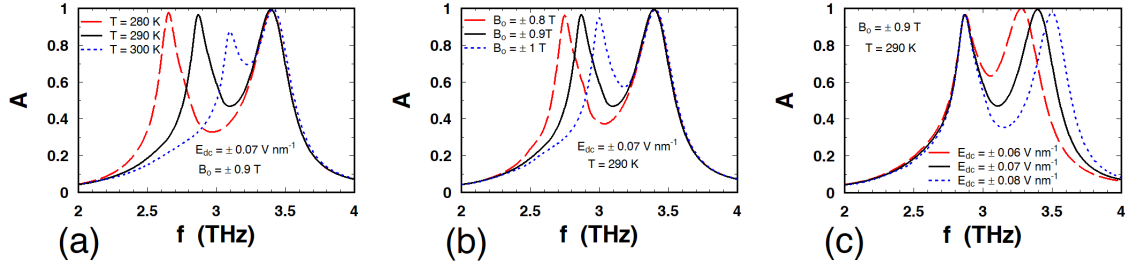


Figure 7: Absorbance A of the metasurface depicted via Fig. 1b as a function of $f \in [2, 4]$ THz, when (a) $T \in \{280, 290, 300\}$ K, $|B_0| = 0.9$ T, and $|E_{dc}| = 0.07$ V nm $^{-1}$; (b) $T = 290$ K, $|B_0| \in \{0.8, 0.9, 1\}$ T, and $|E_{dc}| = 0.07$ V nm $^{-1}$; and (c) $T = 290$ K, $|B_0| = 0.9$ T, and $|E_{dc}| \in \{0.06, 0.07, 0.08\}$ V nm $^{-1}$. These data were computed for $\varphi = 0^\circ$.

Thermal control modality

If T is reduced to 280 K from the quiescent point, the maximum-absorbance frequency of the low-frequency feature redshifts to 2.65 THz and the FWHM bandwidth alters to 0.25 THz in Fig. 7a. In the same figure, the maximum-absorbance frequency of the low-frequency feature changes to 3.09 THz and the FWHM bandwidth to 0.56 THz, if T is increased to 300 K from the quiescent point. Thus, the maximum-absorbance frequency of the low-frequency feature blueshifts at the average rate of 0.022 THz K $^{-1}$ as the temperature increases by 20 K. The maximum absorbance diminishes from 0.97 at $T = 280$ K to 0.87 THz at $T = 300$ K.

For the high-frequency feature, the maximum-absorbance frequency is 3.38 THz at $T = 280$ K and 3.41 THz at $T = 300$ K. The FWHM bandwidth remains about 0.35 THz and the maximum absorbance does not decrease below 0.985, despite the temperature change. Thus, the maximum-absorbance frequency of the high-frequency feature in Fig. 7a blueshifts at the average rate of 0.0015 THz K $^{-1}$ as the temperature increases by 20 K.

We conclude that temperature can be used for: (i) coarse control of the low-frequency peak-shaped fea-

ture and (ii) ultrafine control of the high-frequency peak-shaped feature. This control modality comes from the six InSb-patched pixels in the meta-atoms of the chosen metasurface.

Magnetic control modality

If $|B_0|$ is reduced to 0.8 T from the quiescent point, the maximum-absorptance frequency of the low-frequency feature redshifts to 2.74 THz and the FWHM bandwidth changes to 0.26 THz in Fig. 7b. On the other hand, if $|B_0|$ is increased to 1 T from the quiescent point, the maximum-absorptance frequency of the low-frequency feature blueshifts to 2.99 THz and the FWHM bandwidth changes to 0.67 THz. Thus, the maximum-absorptance frequency of the low-frequency feature blueshifts at the average rate of 1.2 THz T^{-1} as the quasistatic magnetic field's magnitude increases by 0.2 T, the maximum absorptance remaining about 0.94 despite that increase.

For the high-frequency feature, the maximum-absorptance frequency is 3.38 THz at $|B_0| = 0.8 \text{ T}$ and 3.40 THz at $|B_0| = 1 \text{ T}$ in Fig. 7b. The FWHM bandwidth is 0.36 THz at $|B_0| = 0.8 \text{ T}$ and 0.67 THz at $|B_0| = 1 \text{ T}$. The maximum absorptance remains in excess of 0.99, despite the increase in the magnitude of the quasistatic magnetic field's magnitude by 0.2 T. Thus, the maximum-absorptance frequency of the high-frequency feature blueshifts at the average rate of 0.01 THz T^{-1} as $|B_0|$ increases by 0.2 T in Fig. 7b.

Accordingly, a quasistatic magnetic field oriented tangentially to the chosen metasurface can be used for: (i) coarse control of the low-frequency peak-shaped feature and (ii) ultrafine control of the high-frequency peak-shaped feature. This control modality comes from the six InSb-patched pixels in the meta-atoms.

Thus, if the magnet providing magnetic control becomes unavailable, the thermal control modality can be used. Conversely, if the heater/cooler unit providing thermal control becomes unavailable, the magnetic control modality can be used. If both modalities are available, both can be operationally hybridized to reduce the energy expended to run the control modalities.

Electrical control modality

If $|E_{dc}|$ is reduced to 0.06 V nm^{-1} from the quiescent point, the maximum-absorptance frequency of the low-frequency feature blueshifts slightly to 2.872 THz and the FWHM bandwidth changes to 0.69 THz in Fig. 7c. In the same figure, the maximum-absorptance frequency of the low-frequency feature redshifts to 2.86 THz and the FWHM bandwidth alters to 0.24 THz, if $|E_{dc}|$ is increased to 0.08 V nm^{-1} from the quiescent point. Thus, the maximum-absorptance frequency of the low-frequency feature redshifts at the average rate of $0.5 \text{ THz V}^{-1} \text{ nm}$ as the magnitude of the quasistatic electric field increases by 0.02 V nm^{-1} . The maximum absorptance remains in excess of 0.96.

For the high-frequency feature, the maximum-absorptance frequency is 3.27 THz at $|E_{dc}| = 0.06 \text{ V nm}^{-1}$ and 3.49 THz at $|E_{dc}| = 0.08 \text{ V nm}^{-1}$. The FWHM bandwidth is 0.69 THz at $|E_{dc}| = 0.06 \text{ V nm}^{-1}$ and 0.32 THz at $|E_{dc}| = 0.08 \text{ V nm}^{-1}$. The maximum absorptance remains in excess of 0.98, even though the magnitude of the quasistatic electric field is increased by 0.02 V nm^{-1} . Thus, the maximum-absorptance frequency of the high-frequency feature in Fig. 7c blueshifts at the average rate of $11 \text{ THz V}^{-1} \text{ nm}$ as $|E_{dc}|$ is increased by 0.02 V nm^{-1} .

Accordingly, a quasistatic electric field oriented normally to the chosen metasurface can be used for: (i) ultrafine control of the low-frequency peak-shaped feature and (ii) coarse control of the high-frequency peak-shaped feature. This control modality comes from the sole graphene-patched pixel in the meta-atoms.

3.4.4 Example No. 2

In Example No. 1 (Sec. 3.3.4.3), either one or two modalities provide coarse control, whereas the remaining modalities provide fine control, of a maximum-absorptance frequency. Through the absorptance spectrums in Figs. 8a–c, we present an example wherein all three modalities provide comparable control.

The quiescent conditions for the operation of the metasurface depicted via Fig. 1b are chosen for Example No. 2 as follows: $T = 310 \text{ K}$, $|B_0| = 0.8 \text{ T}$, and $|E_{dc}| = 0.07 \text{ V nm}^{-1}$. According to the black solid curves in

Fig. 8, the maximum absorbance is 0.99, the maximum-absorbance frequency is 3.44 THz, and the FWHM bandwidth is 0.47 THz.

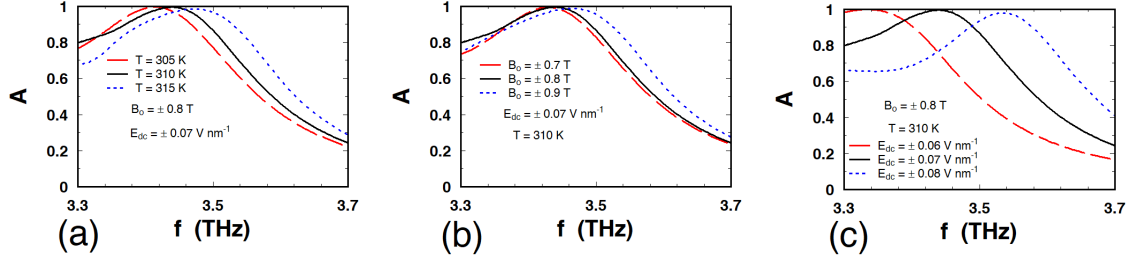


Figure 8: Absorbance A of the metasurface depicted via Fig. 1b as a function of $f \in [3.3, 3.7]$ THz, when (a) $T \in \{305, 310, 315\}$ K, $|B_0| = 0.8$ T, and $|E_{dc}| = 0.07$ V nm $^{-1}$; (b) $T = 310$ K, $|B_0| \in \{0.7, 0.8, 0.9\}$ T, and $|E_{dc}| = 0.07$ V nm $^{-1}$; and (c) $T = 310$ K, $|B_0| = 0.8$ T, and $|E_{dc}| \in \{0.06, 0.07, 0.08\}$ V nm $^{-1}$. These data were computed for $\varphi = 0^\circ$.

When T is changed from 305 K to 315 K but both $|B_0| = 0.8$ T and $|E_{dc}| = 0.07$ V nm $^{-1}$ remain invariant, Fig. 8a shows that the maximum-absorbance frequency blueshifts from 3.41 THz to 3.47 THz at the approximate rate of 0.006 THz K $^{-1}$, and the FWHM bandwidth reduces from 0.54 THz to 0.45 THz, but the maximum absorbance remains at least 0.98.

When $|B_0|$ is changed from 0.7 T to 0.9 T but both $T = 310$ K and $|E_{dc}| = 0.07$ V nm $^{-1}$ are held fixed, Fig. 8b shows that the maximum-absorbance frequency blueshifts from 3.43 THz to 3.46 THz at the approximate rate of 0.15 THz T $^{-1}$, and the FWHM bandwidth reduces from 0.51 THz to 0.44 THz, but the maximum absorbance remains at least 0.98.

Finally, when $|E_{dc}|$ is changed from 0.06 V nm $^{-1}$ to 0.08 V nm $^{-1}$ but both $T = 310$ K and $|B_0| = 0.8$ T are held fixed, Fig. 8c shows that the maximum-absorbance frequency blueshifts from 3.33 THz to 3.53 THz at the approximate rate of 10 THz V $^{-1}$ nm, and the FWHM bandwidth reduces from 0.51 THz to 0.49 THz, but the maximum absorbance remains at least 0.98.

Thus, either of the three control modalities can be employed to tune the maximum-absorbance frequency with comparable degree of control.

3.4.5 Mechanical control modality

There is a fourth control modality available too! Suppose that the polarization angle φ is changed from 0° . The absorbance spectrum will change.

As an example, the absorbance spectrums drawn for Example No. 2 in Sec. 3.4.4 were recalculated for $\varphi = 90^\circ$. With the quiescent conditions $T = 310$ K, $|B_0| = 0.8$ T, and $|E_{dc}| = 0.07$ V nm $^{-1}$ being the same as with $\varphi = 0^\circ$ (Fig. 8), the maximum absorbance remains 0.99 but the maximum-absorbance frequency changes to 3.42 THz and the FWHM bandwidth to 0.43 THz when φ is changed to 90° (Fig. 9). This amounts to fine control exerted through rotation of the incident plane wave by 90° . Similar changes occur when T , $|B_0|$, and $|E_{dc}|$ are changed additionally. Therefore, the lack of rotational invariance of the metasurface depicted via Fig. 1b about the z axis facilitates a mechanical control modality.

4 Concluding Remarks

The pixelated-metasurface approach [30] was inspired by examples from biology in order to design metasurfaces whose electromagnetic response characteristics can be controlled by several different agencies. Theory had previously shown [31] that thermal and magnetic control modalities would be effective for a bicontrollable metasurface comprising pixels patched with CdTe for thermal control and InAs for magnetic control. In this paper, we have presented a tricontrollable metasurface comprising pixels patched with graphene for

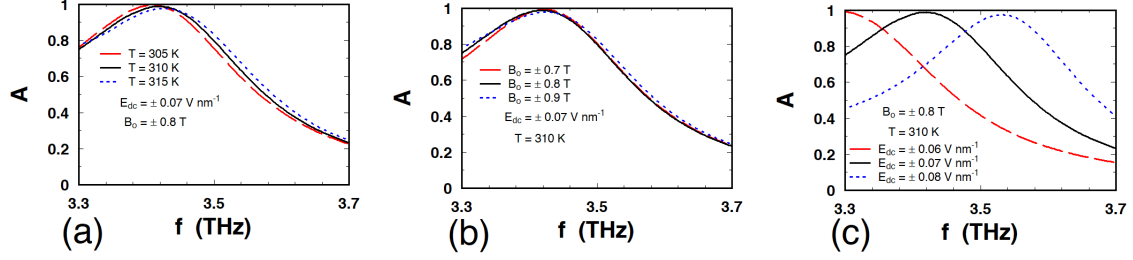


Figure 9: Same as Fig. 8, except for $\varphi = 90^\circ$.

electrical control and InSb for thermal and magnetic control. The lack of rotational invariance of the optimal meta-atom comprising unpatched, graphene-patched, and InSb-patched pixels adds mechanical rotation as the fourth control modality. With microlithographic techniques entailing physical and chemical vapor depositions over a series of masks combined with etching [46, 47] available to fabricate such metasurfaces, we expect that our theoretical efforts will inspire experimentalist colleagues.

Acknowledgments. AL and PKJ thank the Visiting Advanced Joint Research (VAJRA) program of the Department of Science and Technology (Government of India) for initially funding their collaborative research. AL thanks the Charles Godfrey Binder Endowment at Penn State for ongoing support of his research activities and the Otto Mønsted Foundation for generous financial support during an extended stay at the Danish Technical University.

References

- [1] X. C. Tong, *Functional Metamaterials and Metadevices* (Springer, 2018).
- [2] N. M. Estakhri and A. Alú, “Recent progress in gradient metasurfaces,” *J. Opt. Soc. Am. B* **33**, A21–A30 (2016).
- [3] N. Yu, P. Genevet, M. A. Kats, F. Aieta, J.-P. Tetienne, F. Capasso, and Z. Gaburro, “Light propagation with phase discontinuities: Generalized laws of reflection and refraction,” *Science* **334**, 333–337 (2011).
- [4] D. Felbacq, “Weak and strong coupling of a quantum emitter with a meta-surface,” *Superlattices and Microstructures* **78**, 79–87 (2015).
- [5] H.-T. Chen, A. J. Taylor, and N. Yu, “A review of metasurfaces: physics and applications,” *Rept. Prog. Phys.* **79**, 076401 (2016).
- [6] S. B. Glybovski, S. A. Tretyakov, P. A. Belov, Y. S. Kivshar, and C. R. Simovski, “Metasurfaces: From microwaves to visible,” *Phys. Rept.* **634**, 1–72 (2016).
- [7] P. H. Siegel, “Terahertz technology,” *IEEE Trans. Microw. Theory Tech.* **50**, 910–928 (2002).
- [8] H. Tao, W. J. Padilla, X. Zhang, and R. D. Averitt, “Recent progress in electromagnetic metamaterial devices for terahertz applications,” *IEEE J. Sel. Top. Quantum Electron.* **17**, 92–101 (2011).
- [9] A. Y. Pawar, D. D. Sonawane, K. B. Erande, and D. V. Derle, “Terahertz technology and its applications,” *Drug Invention Today* **5**, 157–163 (2013).
- [10] İ. O. Yıldırım, V. A. Özkan, F. İdikut, T. Takan, A. B. Şahin, and H. Altan, “Characterization of a terahertz wave scanned imaging system for threat detection at standoff distances,” *Opt. Quantum Electron.* **48**, 367 (2016).

- [11] J. Qin, L. Xie, and Y. Ying, “A high-sensitivity terahertz spectroscopy technology for tetracycline hydrochloride detection using metamaterials,” *Food Chem.* **211**, 300–305 (2016).
- [12] S. K. Yngvesson, A. Karellas, S. Glick, A. Khan, P. R. Siqueira, P. A. Kelly, and B. Saint Peter, “Breast cancer margin detection with a single frequency terahertz imaging system,” *Proc. SPIE* **9706**, 970603 (2016).
- [13] S. Thongrattanasiri, F. H. L. Koppens, and F. J. García de Abajo, “Complete optical absorption in periodically patterned graphene,” *Phys. Rev. Lett.* **108**, 047401 (2012).
- [14] X. Huang, X. Zhang, Z. Hu, M. Aqeeli, and A. Alburaikan, “Design of broadband and tunable terahertz absorbers based on graphene meta-surface: equivalent circuit model approach,” *IET Microw. Antennas Propagat.* **9**, 307–312 (2015).
- [15] X. Liu, K. Fan, I. V. Shadrivov, and W. J. Padilla, “Experimental realization of a terahertz all-dielectric metasurface absorber,” *Opt. Express* **25**, 191–201 (2017).
- [16] C. Liu, L. Qi, and M. Wu, “Triple-broadband infrared metamaterial absorber with polarization-independent and wide-angle absorption,” *Opt. Mater. Express* **8**, 2439–2448 (2018).
- [17] P. Kumar, A. Lakhtakia, and P. K. Jain, “Graphene-pixel-based polarization-insensitive metasurface for almost perfect and wideband terahertz absorption,” *J. Opt. Soc. Am. B* **36**, F84–F88 (2019).
- [18] P. Kumar, A. Lakhtakia, and P. K. Jain, “Graphene-pixel-based polarization-insensitive metasurface for almost perfect and wideband terahertz absorption: erratum,” *J. Opt. Soc. Am. B* **36**, 1914 (2019).
- [19] R. A. Depine, *Graphene Optics: Electromagnetic Solution of Canonical Problems* (Morgan & Claypool, 2016).
- [20] A. H. Castro Neto, F. Guinea, N. M. R. Peres, K. S. Novoselov, and A. Geim, “The electronic properties of graphene,” *Rev. Modern Phys.* **81**, 109–162 (2009).
- [21] G. W. Hanson, “Dyadic Green’s functions for an anisotropic, non-local model of biased graphene,” *IEEE Trans. Antennas Propagat.* **56**, 747–757 (2008).
- [22] R. Wang, X.-G. Ren, Z. Yan, L.-J. Jiang, W. E. I. Sha, and G.-C. Shan, “Graphene-based functional devices: A short review,” *Front. Phys.* **14**, 13603 (2019).
- [23] J. Liu, A. R. Wright, C. Zhang, and Z. Ma, “Strong terahertz conductance of graphene ribbons under a magnetic field,” *Appl. Phys. Lett.* **93**, 041106 (2008).
- [24] C. Kittel, *Introduction to Solid State Physics* (Wiley Eastern, 1974).
- [25] R. W. Cunningham and J. B. Gruber, “Intrinsic concentration and heavy-hole mass in InSb,” *J. Appl. Phys.* **41**, 1804–1809 (1970).
- [26] M. Oszwaldowski and M. Zimpel, “Temperature dependence of intrinsic carrier concentration and density of states effective mass of heavy holes in InSb,” *J. Phys. Chem. Solids* **49**, 1179–1185 (1988).
- [27] J. J. Brion, R. F. Wallis, A. Hartstein, and E. Burstein, “Theory of surface magnetoplasmons in semiconductors,” *Phys. Rev. Lett.* **28**, 1455–1458 (1972).
- [28] H. C. Chen, *Theory of Electromagnetic Waves* (McGraw–Hill, 1983).
- [29] J. Han, A. Lakhtakia, Z. Tian, X. Lu, and W. Zhang, “Magnetic and magnetothermal tunabilities of subwavelength-hole arrays in a semiconductor sheet,” *Opt. Lett.* **34**, 1465–1467 (2009).

- [30] A. Lakhtakia, D. E. Wolfe, M. W. Horn, J. Mazurowski, A. Burger, and P. P. Banerjee, “Bioinspired multicontrollable metasurfaces and metamaterials for terahertz applications,” *Proc. SPIE* **10162**, 101620V (2017).
- [31] F. Chiadini and A. Lakhtakia, “Bicontrollable terahertz metasurface with subwavelength scattering elements of two different materials,” *Appl. Opt.* **57**, 189–196 (2018).
- [32] S. Clemens, M. F. Iskander, Z. Yun, and J. Rayno, “Hybrid genetic programming for the development of metamaterials designs with improved characteristics,” *IEEE Antennas Wireless Propagat. Lett.* **17**, 513–516 (2018).
- [33] D. Cvijović, “New integral representations of the polylogarithm function,” *Proc. R. Soc. Lond. A* **463**, 897–905 (2007).
- [34] Y. Jaluria, *Computer Methods for Engineering* (Taylor & Francis, 1996).
- [35] K. S. Novoselov, A. K. Geim, S. V. Morozov, D. Jiang, M. I. Katsnelson, I. V. Grigorieva, S. V. Dubonos, and A. A. Firsov, “Two-dimensional gas of massless Dirac fermions in graphene,” *Nature* **438**, 197–200 (2005).
- [36] S. Wu and J. S. Li, “Hollow-petal graphene metasurface for broadband tunable THz absorption,” *Appl. Opt.* **58**, 3023–3028 (2019).
- [37] X. G. Peralta, C. L. Arrington, J. D. Williams, A. Strikwerda, R. D. Averitt, W. J. Padilla, J. F. O’Hara, and I. Brener, “Terahertz metamaterials on thin silicon nitride membranes,” *Mater. Res. Soc. Symp. Proc.* **1077**, 1077-L07-18 (2008).
- [38] M. J. Grieco, F. L. Worthing, and B. Schwartz, “Silicon nitride thin films from SiCl_4 plus NH_3 : Preparation and properties,” *J. Electrochem. Soc.: Solid State Sci.* **115**, 525–531 (1968).
- [39] M. N. O. Sadiku, *Elements of Electromagnetics* (Oxford University Press, 2000).
- [40] C. F. Bohren and D. R. Huffman, *Absorption and Scattering of Light by Small Particles* (Wiley, 1983).
- [41] G. Cataldo, J. A. Beall, H.-M. Cho, B. McAndrew, M. D. Niemack, and E. J. Wollack, “Infrared dielectric properties of low-stress silicon nitride,” *Opt. Lett.* **37**, 4200–4202 (2012).
- [42] A. Lakhtakia, S. Bhattacharyya, and S. K. Ghosh, “Comment on: ‘Wide incidence angle and polarization insensitive dual broad-band metamaterial absorber based on concentric split and continuous rings resonator structure’,” *Mater. Res. Express* **6**, 088002 (2019).
- [43] C. S. R. Kaipa, A. B. Yakovlev, G. W. Hanson, Y. R. Padooru, F. Medina, and F. Mesa, “Enhanced transmission with a graphene-dielectric microstructure at low-terahertz frequencies,” *Phys. Rev. E* **85**, 245407 (2012).
- [44] P. C. Wu, N. Papasimakis, and D. P. Tsai, “Self-affine graphene metasurfaces for tunable broadband absorption,” *Phys. Rev. Appl.* **6**, 044019 (2016).
- [45] M. Rahmanzadeh, A. Abdolali, A. Khavasi, and H. Rajabalipanah, “Adopting image theorem for rigorous analysis of a perfect electric conductor-backed array of graphene ribbons,” *J. Opt. Soc. Am. B* **35**, 1836–1844 (2018).
- [46] S. Franssila, *Introduction to Microfabrication*, 2nd ed. (Wiley, 2010).
- [47] R. J. Martín-Palma and A. Lakhtakia, *Nanotechnology: A Crash Course* (SPIE Press, 2010).